Journal of Materials Chemistry A

Elucidating the mechanism of perovskite surface passivation with organic molecules: the impact of π-conjugation length

Journal:	*Journal of Materials Chemistry A*
Manuscript ID	TA-ART-01-2025-000754.R1
Article Type:	Paper
Date Submitted by the Author:	19-Apr-2025
Complete List of Authors:	Koseki, Daichi; Kyushu University; The University of Tokyo Graduate School of Arts and Sciences College of Arts and Sciences Senevirathne, Chathuranganie; Kyushu University Senba, Dai; Kyushu University Fujita, Yuki; Kyushu University Lin, Jun; Kyushu University International Institute for Carbon-neutral Energy Research Zhai, Mengde; Kyushu University International Institute for Carbon-neutral Energy Research Shang, Juan; Kyushu University International Institute for Carbon-neutral Energy Research Raju, Telugu; Kyushu University Ida, Shintaro; Kumamoto University, Graduate School of Science and Technology Watanabe, Motonori; Kyushu University, International Institute for Carbon-Neutral Energy Research Staykov, Aleksandar; Kyushu University International Institute for Carbon-neutral Energy Research Segawa, Hiroshi; The University of Tokyo, Komaba Research Campus, Research Center for Advanced Science and Technology (RCAST) Guo, Zhanglin; Kyushu University, Matsushima, Toshinori; Kyushu University, International Institute for Carbon-Neutral Energy Research

ARTICLE

Elucidating the mechanism of perovskite surface passivation with organic molecules: the impact of π-conjugation length

Received 00th January 20xx,
Accepted 00th January 20xx

DOI: 10.1039/x0xx00000x

Daichi Koseki,[abc] Chathuranganie A. M. Senevirathne,[a] Dai Senba,[ad] Yuki Fujita,[ab] Jun Lin,[ad] Mengde Zhai,[ade] Juan Shang,[a] Telugu Bhim Raju,[a] Shintaro Ida,[fg] Motonori Watanabe,[abdg] Aleksandar Staykov,[abg] Hiroshi Segawa,[ch] Zhanglin Guo,[adg] Toshinori Matsushima*[abdg]

To further enhance the performance of perovskite solar cells (PSCs), a more comprehensive analysis of the mechanisms through which organic molecules induce defect passivation and enhance hole extraction is essential. In this study, we employ several organic molecules with varying π-conjugation lengths to examine how factors such as their molecular desorption, energy levels, and radical-cation stability affect defect passivation, hole extraction, and the overall PSC performance. Our results show that passivation molecules with extended π-conjugation suppress molecular desorption from the perovskite surfaces during overlayer spin-coating and improve energy-level alignment at interfaces, thereby enhancing PSC efficiency through improved defect passivation and hole extraction. Additionally, extended π-conjugation improves radical-cation stability, contributing to greater device durability. Among the defect passivation materials studied, 2-(3-ethlylamine)benzothieno[3,2-b]benzothiophene, hydroiodide (BTBTAI) can provide the most significant improvements in these factors, increasing the initial efficiency from 22.7% to 24.6% and raising the efficiency retention from 61% to 85% after 1,000 hours of continuous light illumination at 25 °C in formamidinium lead iodide-based PSCs. Reports on defect passivation from the perspectives of molecular desorption and cation stability are extremely limited. Therefore, these findings deepen the understanding of PSC operating mechanisms and offer valuable insights for developing design guidelines for future defect passivation materials with even higher device performance.

1 Introduction

Over the past decade, halide perovskite solar cells (PSCs) have made remarkable strides in power conversion efficiency (PCE). Recently, certified PCEs for single-junction PSCs have exceeded 27%,[1] achieving performance levels comparable to silicon-based technology. These PCE improvements are largely attributed to advancements in defect passivation techniques, control over crystal growth and phase distribution in the perovskite layers, and the development of excellent charge carrier transport materials.[2–7] In addition to the efficiency improvements, significant efforts have focused on improving PSC durability for practical applications, particularly under challenging conditions such as prolonged illumination, thermal cycling, and damp heat.[8–10] Attaining such exceptional PSC efficiency and durability necessitates efficient charge extraction and the minimization of non-radiative recombination at the interfaces between the perovskite layer and the adjoining charge-transport layers. [6,7,11,12]

Various defects, including antisites, interstitials, vacancies, impurities, and dangling bonds, exist at perovskite surfaces and grain boundaries.[13,14] These defects promote non-radiative charge carrier recombination, which reduces quasi-Fermi level splitting and increases voltage loss.[15,16] Passivating these defects, especially at the interface between the perovskite layer and the hole transport layer (HTL) in n-i-p PSC architectures, is crucial for mitigating recombination, improving durability, and enhancing resistance to moisture and thermal stress.[4,6,7,11,12,17,18] Effective passivation materials are Lewis acids and Lewis bases, and they often feature anchoring groups, such as amines, phosphonic acid, sulfonic acid, carboxylic acid, and so on.[11,17,19–24] Widely used amine-based passivation materials are 2-phenylethylamine hydroiodide (PEAI) and *n*-octylammonium iodide (OAI), which help compensate for ion vacancies.[7,11,24–27] However, these and other reported passivation materials often behave as insulating layers with poor hole extraction capabilities due to unfavorable energy level alignment, which negatively impacts overall device performance.[28–31] To overcome this challenge, research has

[a] International Institute for Carbon-Neutral Energy Research (WPI-I2CNER), Kyushu University, Fukuoka 819-0395, Japan. E-mail: tmatusim@i2cner.kyushu-u.ac.jp
[b] Department of Applied Chemistry, Faculty of Engineering, Kyushu University, Fukuoka 819-0395, Japan.
[c] Department of General Systems Studies, Graduate School of Arts and Sciences, The University of Tokyo, Tokyo 153-8902, Japan.
[d] Department of Automotive Science, Graduates School of Integrated Frontier Sciences, Kyushu University, 744 Motooka, Nishi, Fukuoka 819-0395, Japan
[e] Institute for Energy Research, School of Energy and Power Engineering, Jiangsu University, Zhenjiang 212013, China
[f] Institute of Industrial Nanomaterials (IINa), Kumamoto University, Kumamoto 860-8555, Japan.
[g] Center for Energy Systems Design (CESD), International Institute for Carbon-Neutral Energy Research (WPI-I2CNER), Kyushu University, Fukuoka 819-0395, Japan
[h] Research Center for Advanced Science and Technology, The University of Tokyo, Tokyo 153-8904, Japan
† Electronic supplementary information (ESI) available. See DOI:

shifted toward developing defect passivation materials with appropriate energy levels or molecular dipoles to enhance hole extraction.[4,32–34] Additionally, the desorption of passivation molecules from perovskite surfaces during overlayer coating from solution remains problematic because it makes obtaining the original defect passivation effects difficult.[35–37] Thus, it is urgently necessary to understand and develop defect passivation materials that offer better energy level alignment and resistance to the molecular desorption.

Under solar illumination, holes generated in the perovskite layer are extracted to the HTL through the defect passivation molecules, resulting in the continuous formation of radical cations in these passivation molecules. Organic radicals are highly reactive species that often participate in single-electron redox processes.[38–41] As key intermediates, they play crucial roles in various organic reactions, such as radical polymerization and organic photocatalysis.[42–44] Consequently, the stability of the radical cations formed from the passivation molecules is believed to be essential for the operational durability of PSCs, as these radicals can potentially interact or react with neighboring materials. Generally, organic radicals can be stabilized by extending π-conjugation because of the radical to delocalize across the molecule,[39,45–47] which is expected to improve PSC durability. However, the stability of radical cations in defect passivation molecules used in PSCs has not been explored in detail.

In this study, we investigate how the PCE and operational durability of PSCs are influenced by the molecular desorption from perovskite surfaces, hole transport energy levels, and radical-cation stability of several defect passivation materials, all sharing the same amine-based anchoring group. For this, we compare four defect passivation materials: 2-phenylethylammonium iodide (PEAI), 1-naphthylmethylamine hydroiodide (NMAI), 9-anthrylmethylamine hydroiodide (AMAI), and 2-(3-ethlylamine)benzothieno[3,2-b]benzothiophene, hydroiodide (BTBTAI) (see Fig. 1a for their molecular structures). PEAI has been widely used for defect passivation in PSCs,[11,24,26,48,49] while NMAI has primarily functioned as a large cation for forming two-dimensional perovskite films,[50] in addition to being used for defect passivation.[51] AMAI and its analogues have not yet been applied to perovskite-based devices for defect passivation. In the course of determining the molecular structure, we attempted to synthesize a material with a more π-conjugated tetracene core. However, due to its extremely low solubility, we were unable to obtain the tetracene-based material in high purity. As an alternative, we developed a BTBTAI material using BTBT as the core structure. An analogue of BTBTAI, with the different number of carbons between the BTBT core and the amino group (three carbons in a previous report compared to two carbons in this study), has been used to create two-dimensional perovskites and fabricate inverted-architecture PSCs;[52–54] however, its role in defect passivation needs to be examined in greater detail, as is done in this study. The BTBT core is known to have efficient hole transport as demonstrated in organic thin-film transistor research.[55,56] These defect passivation materials, with varying π-conjugation lengths, exhibit systematically different molecular desorption, energy-level alignment, and radical-cation stability, making them well-suited for evaluating their impact on device performance.

Here we show that increasing the π-conjugation lengths—progressing from PEAI to NMAI, AMAI, and BTBTAI—improves device performance. As π-conjugation lengths increase, solubility in organic solvents decreases and intermolecular π–π stacking is enhanced, suppressing the desorption of defect passivation molecules from perovskite surfaces during the spin-coating of the chemically doped 2,2',7,7'-tetrakis-(*N*,*N*-di-4-methoxyphenylamino)-9,9'-spirobifluorene (spiro-OMeTAD) HTL, thereby preserving the original defect passivation ability. Defect passivation molecules with extended π-conjugation have shallower hole transport energy levels, promoting hole extraction by reducing energy-level mismatches at interfaces. This enhancement in both defect passivation and hole extraction leads to improved PCE of PSCs. Moreover, a correlation between π-conjugation and operational durability is likely, with defect passivation molecules featuring extended π-conjugation demonstrating greater durability. This is in part because the radical cations of passivation molecules with longer π-conjugation lengths are more stable. Overall, the highest device performance is achieved with BTBTAI-based defect passivation because of suppressed molecular desorption, better energy level alignment, and higher radical-cation stability. This leads to an increase in initial PCE from 17.6% to 20.2% and an improvement in efficiency retention from 49% to 80% after 1,000 hours of continuous light illumination at 25°C for mixed cation perovskite-based PSCs. Furthermore, with BTBTAI treatment, a PCE increase from 22.7% to 24.6% and a retention improvement from 61% to 85% under the same durability measurement condition are achieved in formamidinium lead iodide ($FAPbI_3$)-based PSCs. Systematic investigations into the relationship between molecular characteristics—particularly molecular desorption and radical-cation stability—, and defect passivation, and charge extraction, and their collective impact on PSC performance have been limited to date, making this study a valuable contribution to advancing the understanding of device physics and guiding the development of defect passivation strategies in PSC research.

2 Experimental

2.1 Materials

SnO_2 colloidal dispersion [15% tin(IV) oxide in water] and NiO_x powder were purchased from Alfa Aesar and Advanced Electronic Technology, respectively. Formamidinium iodide (FAI), methylammonium bromide (MABr), methylammonium chloride (MACl), cesium iodide (CsI), lead iodide (PbI_2), lead bromide ($PbBr_2$), phenethylammonium iodide (PEAI), 1-naphthylmethylamine (NMA), hydroiodic acid (HI), and 4-(3,6-dimethyl-9H-carbazol-9-yl)butyl]phosphonic acid (Me-4PACZ) were obtained from Tokyo Chemical Industry. Spiro-OMeTAD, 2,9-dimethyl-4,7-diphenyl-1,10-phenanthroline (BCP), fullerene (C_{60}), chlorobenzene (CB), *N*,*N*-dimethylformamide (DMF), dimethyl sulfoxide (DMSO), ethanol

(EtOH), anisole, potassium hydroxide (KOH), lithium bis(trifluoromethanesulfonyl)imide (LiTFSI), tris(2-(1H-pyrazol-1-yl)-4-tert-butylpyridine)cobalt(III) tris(bis(trifluoromethylsulfonyl)imide (FK-209), 4-tert-butylpyridine (4-tBP), and 2,7-dioctyl[1]benzothieno[3,2-b][1];2,7-dioctyl[1]benzothieno[3,2-b][1]benzothiophene (C8-BTBT) were purchased from Sigma-Aldrich. MoO_3 was sourced from Mitsuwa Chemical. Isopropanol (IPA) and acetonitrile (ACN) were purchased from Wako Pure Chemical. All the materials were used as received without further purification. NMAI was synthesized through a simple reaction between NMA and HI. For this synthesis, NMA and HI were mixed in a 1:1 molar ratio in toluene under nitrogen, and stirred for 90 minutes to complete the reaction. The resulting white powder was filtered under reduced pressure and purified twice by recrystallization. AMA in the non-iodide form was synthesized according to the synthetic routes provided in the Supporting Information (Fig. S1–S4 †). Then, AMAI was obtained from AMA in the same way used for the NMAI synthesis. BTBTAI was synthesized according to the synthetic routes provided in the Supporting Information (Fig. S5–S13 †).

2.2 Substrate cleaning

Glass substrates coated with a pre-patterned indium tin oxide (ITO) layer (~150 nm thick with a sheet resistance of ~10 Ω sq^{-1}, or ~100 nm thick with a sheet resistance of ~15 Ω sq^{-1}, Atsugi Micro) or fused silica substrates were sequentially cleaned by ultrasonication. The cleaning process involved ultrasonication in detergent, pure water, acetone, and isopropanol, each for 15 minutes. Following this, the substrates were subjected to UV–ozone treatment for 15 minutes.

2.3 Preparation of precursor solution

In this paper, the composition $Cs_{0.05}(FA_{0.85}MA_{0.15})_{0.95}Pb(I_{0.85}Br_{0.15})_3$ is referred to as "mixed cation". For the mixed cation-based perovskite fabrication, the precursor solution was prepared by mixing 1.10 M FAI, 0.20 M MABr, 1.15 M PbI_2, and 0.20 M $PbBr_2$ in an anhydrous DMF/DMSO mixture (at a 9:1 volume ratio). Additionally, 0.08 M CsI solution in DMSO was added to this solution. The resulting solution was stirred at 70°C for 1 hour, then filtered using a 0.2 µm polytetrafluoroethylene (PTFE) filter prior to use. For the $FAPbI_3$-based perovskite fabrication, 691 mg of PbI_2 was dissolved in 1 mL of an anhydrous DMF/DMSO mixture (at a 9:1 volume ratio). The mixed organic salt precursor solution was prepared by dissolving 90 mg of FAI and 12 mg of MACl in 1 mL of IPA. These two solutions were stirred at 25°C for 12 hours. For the spiro-OMeTAD HTL fabrication, 36.5 mg of spiro-OMeTAD was dissolved in 0.5 mL of CB. This solution was then mixed with 9 µL of LiTFSI stock solution (520 mg mL^{-1} in ACN), 14.5 µL of FK-209 stock solution (300 mg mL^{-1} in ACN), and 15 µL of 4-tBP. The spiro-OMeTAD solution was also filtered using a 0.2 µm PTFE filter before use. The defect passivation solution was prepared by dissolving PEAI, NMAI, AMAI, or BTBTAI in EtOH at a predetermined concentration, typically 1 mM unless otherwise specified.

2.4 Sample fabrication

The PSC architecture fabricated in this study was glass substrate/ITO (~150 nm) electrode/SnO_2 electron transport layer (ETL; ~30 nm)/mixed cation (650 nm) or $FAPbI_3$ (~750 nm)-based perovskite light absorber/chemically doped spiro-OMeTAD HTL (~150 nm)/Au electrode (~80 nm) (Fig. 1b). The values in the parentheses in these device architectures indicate the thicknesses of each layer. The SnO_2 ETL was prepared by spin-coating a SnO_2 colloidal dispersion (diluted 1:3 with pure water) at 3,000 rpm for 30 s, followed by annealing at 150°C for 30 minutes and UV–ozone treatment for 15 minutes. To further enhance performance for mixed cation-based PSCs, the SnO_2 surface was treated by spin-coating a 1 mM KOH aqueous solution at 3,000 rpm for 30 s, followed by annealing at 100°C for 10 minutes.[57] For the mixed cation-based perovskite fabrication, the perovskite precursor layer was deposited on the KOH-treated ITO surface by spin-coating at 1,000 rpm for 10 s, then at 6,000 rpm for 30 s. Ten seconds before the end of this process, 120 µL of CB was dropped onto the spinning substrate. The perovskite precursor layer was then annealed at 100°C for 30 minutes to complete its conversion to the mixed cation-based perovskite. In separate experiments, the $FAPbI_3$-based perovskite layer was prepared using a two-step deposition method. First, the PbI_2 layer was spin-coated from the PbI_2 solution at 1,500 rpm for 30 seconds and annealed at 70°C for 1 minute. Next, the mixed FAI:MACl layer was spin-coated at 1,800 rpm for 30 seconds onto the PbI_2 layer, followed by annealing at 150°C for 15 minutes under an ambient air condition (20–30% relative humidity) for its conversion to the $FAPbI_3$-based perovskite. The surfaces of the mixed cation- and $FAPbI_3$-based perovskite layers were treated by spin-coating with a PEAI, NMAI, AMAI, or BTBTAI solution at 4,000 rpm for 30 seconds. The chemically doped spiro-OMeTAD HTL was subsequently fabricated on the perovskite layers by spin-coating at 4,000 rpm for 30 seconds. The SnO_2 ETL fabrication and KOH treatment were performed in dry air, whereas the other layers were prepared in a nitrogen environment, except for the annealing of the $FAPbI_3$ layers, which was carried out in the humidity-controlled air. Finally, an Au electrode was thermally deposited under vacuum (base pressure ~10^{-4} Pa) at a deposition rate of ~0.1 nm s^{-1}. The inverted PSCs with the architecture glass substrate/ITO/NiO_x/Me-4PACz/$Cs_{0.05}FA_{0.8}MA_{0.15}PbI_{2.25}Br_{0.75}$ perovskite/C_{60}/BCP/Ag were fabricated under exactly the same conditions as those reported in the literature.[58] The fabricated PSCs were encapsulated using a glass lid, UV-curing sealant, and a desiccant sheet, all without exposure to air.

2.5 Sample characterization

Current density–voltage (*J*–*V*) measurements were performed on PSCs using a computer-controlled Keysight B2901A source/measure unit under simulated solar illumination (AM1.5G, 100 mW cm^{-2}) provided by a Xe lamp-based solar simulator (HAL-320, Asahi Spectra). The active area of the PSCs was defined as 0.095 cm^2 using a black shadow mask, while the original device area, defined by the overlap of the ITO and Au electrodes, was 0.12 cm^2. Prior to *J*–*V* measurements, the lamp power was calibrated to 100 mW cm^{-2} using a crystalline silicon reference cell with an amorphous Si optical filter (Bunkokeiki), certified by the National Institute of Advanced Industrial Science and Technology. Maximum power point tracking (MPPT) to evaluate stabilized PCE was conducted using the same

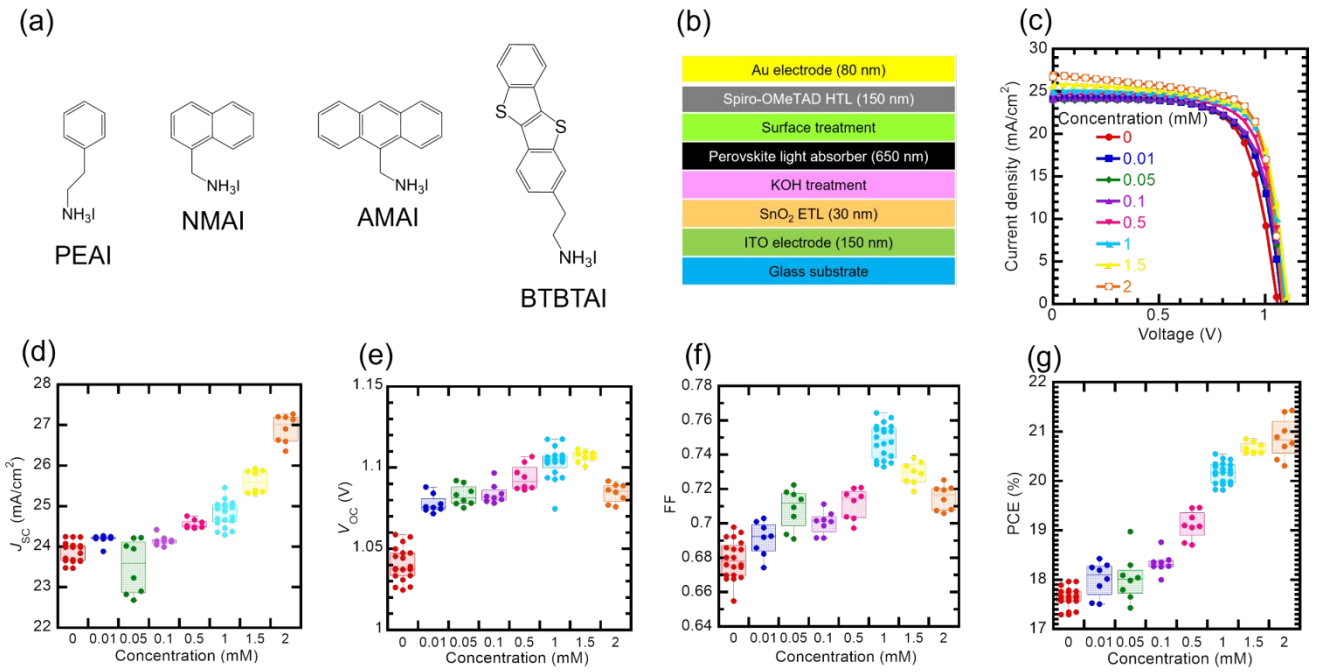

Fig. 1 (a) Chemical structures of PEAI, NMAI, AMAI, and BTBTAI. (b) Schematic PSC architecture. (c) Representative illuminated *J*–*V* curves and plots of (d) J_{SC}, (e) V_{OC}, (f) FF, and (g) PCE for mixed cation-based PSCs treated by spin-coating with BTBTAI solutions at different concentrations.

setup. Incident-photon-to-current efficiency (IPCE) curves of PSCs were obtained with the Keysight B2901A source/measure unit and a constant-energy monochromatic light source (PVL-5000, Asahi Spectra). To calculate IPCE, the monochromatic light energy was measured using a power meter (843-R, Newport) and an optical power detector (818-UV/DB, Newport). For transient photovoltage (TPV) and photocurrent (TPC) measurements, the PSCs were connected to a digital oscilloscope (DS-5110B, Iwatsu Electronic) using a BNC cable. A square-shaped illumination from a high-speed white LED (FOLS-10, Sawaki), driven by a pulse generator unit (PGU-100k, Sawaki), was used with an illumination intensity of 100 mW cm^{-2} and a pulse width of 50 ms. The oscilloscope's input impedance was set to 100 kΩ for TPV decays and 50 Ω for TPC decays. Cross-sectional scanning electron microscope (SEM) images of the PSCs, prepared by breaking the substrates into small pieces, were obtained using Hitachi JSM-7900F. The operational durability of the encapsulated PSCs was evaluated under 100 mW cm^{-2} illumination from 3000 K white LEDs with the MPPT at 25 °C (PAS-100, System Engineers).

Steady-state photoluminescence (PL) spectra and time-resolved transient PL decays of the perovskite, PEAI, NMAI, AMAI, and BTBTAI films were measured using a steady-state PL spectrometer (FP-8300, JASCO) and a PL lifetime spectrometer (Quantaurus-Tau, Hamamatsu Photonics), respectively. Surface morphology and structural characterization of the perovskite films were performed using a SEM (JSM-7900F, JEOL) and an X-ray diffractometer (XRD; SmartLab 9kW AMK, Rigaku) with the standard two theta/theta technique [λ = 1.54 Å (CuKα)], respectively. Grazing incidence XRD (GIXRD) was also performed on the perovskite films using the same equipment, with an incidence angle of 1°. UV-VIS absorption spectra of the perovskite, PEAI, NMAI, AMAI, and BTBTAI films were recorded using an absorption spectrometer (V-730, JASCO). Photoelectron yield spectroscopy (PYS; AC-2, Rikenkeiki) was employed to measure the hole transport energy levels of the materials, including the highest occupied molecular orbital (HOMO) energy levels for organics and the valence band edge energy levels for inorganics. To prevent surface charge accumulation during PYS measurements, the sample films were prepared on ITO-coated glass substrates. The electronic states of untreated and surface-treated perovskite films were characterized by X-ray photoelectron spectroscopy (XPS; PHI5000, VersaProbe II) using a monochromatic Al Kα source (1486.6 eV). Binding energies were calibrated using the Au $4f_{7/2}$ peak (84.0 eV) measured from a vacuum-deposited Au sample.

The optimized structures of the defect passivation molecules were calculated using Gaussian 16, Revision C.01. Geometry optimizations were carried out with the B3LYP functional and 6-31+G(d) basis set, and no imaginary frequencies were observed, confirming that the structures correspond to energy minima. The HOMO orbitals were visualized using GaussView 6.1.1 with an isovalue of 0.02. The molecular assembly states and corresponding binding energies on the $FAPbI_3$ perovskite surface were calculated under the reported conditions.[37]

2.6 Hole-only device fabrication and characterization

To investigate the stability of the organic radical-cation states, hole-only devices (HODs) were fabricated with the following architecture: glass substrate/ITO (100 nm)/MoO_x (10 nm)/PEAI, NMAI, AMAI, or BTBTAI (200 nm)/MoO_x (10 nm)/Au (80 nm). The values in the parentheses in the HOD architectures indicate the thicknesses of

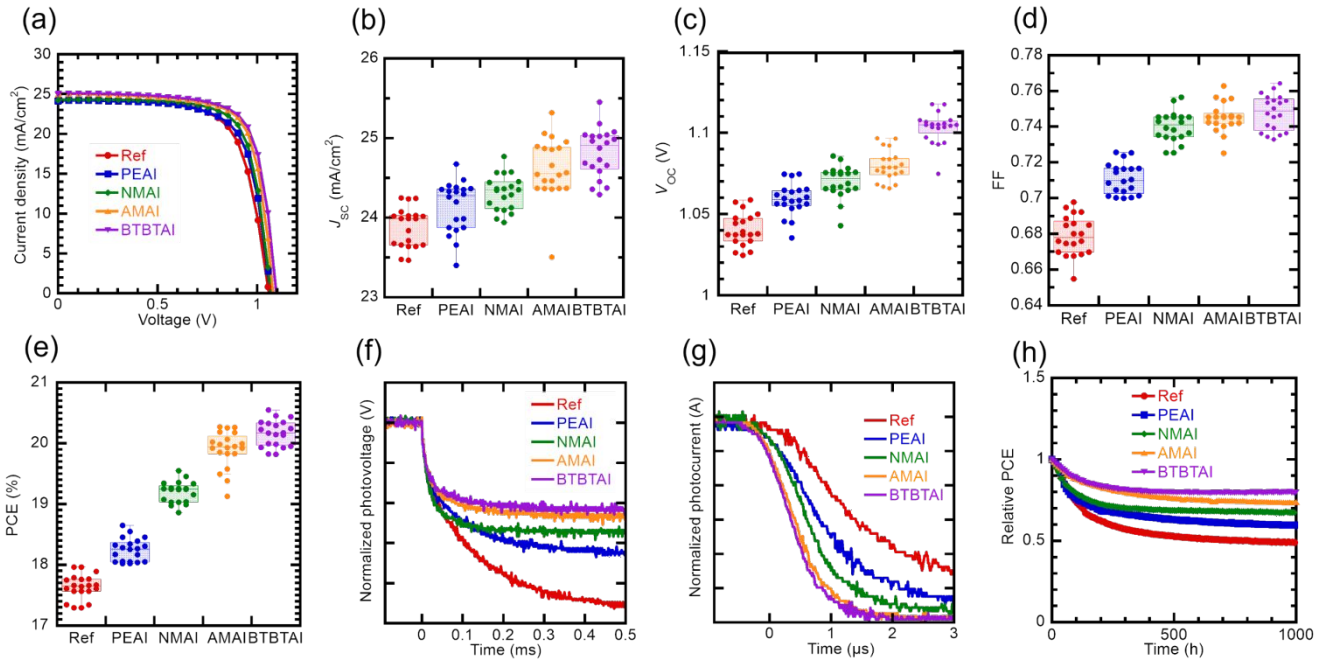

Fig. 2 (a) Representative illuminated *J*–*V* curves, plots of (b) J_{SC}, (c) V_{OC}, (d) FF, and (e) PCE, (f) TPV and (g) TPC decays, and (h) PCE evolution under the continuous illumination with MPPT at 25 °C for mixed cation-based PSCs treated by spin-coating with 1 mM PEAI, NMAI, AMAI, or BTBTAI solutions.

each layer. All the layers were vacuum-deposited onto the ITO surface at a pressure of ~10^{-4} Pa, with deposition rates of ~0.05 nm s^{-1} for MoO_x and ~0.1 nm s^{-1} for the organics and Au. While the original source material was MoO_3, the vacuum-deposited films contained numerous oxygen vacancies, yielding MoO_x, where *x* is lower than 3.[59] The device area, defined by the overlap between the ITO and Au, was 4 mm^2. Voltage evolution of the encapsulated HODs was monitored over time under constant current density operation at 25 mA cm^{-2} using a DC voltage current source/monitor meter (6241C, ADCMT).

3 Results and discussion

3.1 Optimization of BTBTAI solution concentration

The concentrations of BTBTAI solutions used for defect passivation were first optimized to achieve maximum PSC device performance. For this, PSCs with the mixed cation-based perovskite layer treated by spin-coating BTBTAI solutions of varying concentrations (0, 0.01, 0.05, 0.1, 0.5, 1, 1.5, or 2 mM) were fabricated and evaluated. Fig. 1c shows the representative *J*–*V* curves of mixed cation-based PSCs measured under the simulated one-sun condition (AM1.5G, 100 mW cm^{-2}) in a reverse bias scan from 1.2 to 0 V. Short-circuit current densities (J_{SC}), open-circuit voltages (V_{OC}), fill factors (FF), and PCEs are plotted as a function of BTBTAI solution concentration in Fig. 1d–g and summarized in Table S1 † . The solar cell parameter values discussed in this paper represent the mean values from multiple devices fabricated across the same or different batches.

As the BTBTAI solution concentration increased from 0 to 1 mM, J_{SC} rose from 23.9 to 24.8 mA cm^{-2}, V_{OC} increased from 1.04 to 1.10 V, and FF improved from 0.68 to 0.75, leading to an increase in PCE from 17.6% to 20.2%. The improved device performance can be attributed to enhanced defect passivation and more efficient hole extraction, probably resulting from increased coverage of the perovskite layer by BTBTAI. However, at higher BTBTAI concentrations (1.5 and 2.0 mM), J_{SC} showed a rapid and unexpected increase. The J_{SC} value at 2.0 mM reached 26.9 mA cm^{-2}, which appears to be overestimated.

In PSCs treated with the 2.0 mM BTBTAI solution, a circular-shaped structure was observed (Fig. S14 †), likely indicating that thick BTBTAI precipitated during spin-coating, as the 2 mM solution was near saturation (Fig. S15 †). We attempted to measure the thickness of the BTBTAI precipitate using atomic force microscopy and laser microscopy. However, the measurements were unsuccessful, possibly because the precipitate was too thin. Alternatively, the BTBTAI layer may not be uniformly flat, which could also hinder accurate thickness measurement. Since the structured BTBTAI was slightly cloudy upon visual inspection, it may cause solar light scattering, artificially increasing the effective illumination area and potentially leading to the overestimated J_{SC}. More specifically, it is assumed that a portion of the solar light that passes through the perovskite layer without being absorbed is scattered by the crystalline BTBTAI precipitate into regions outside the shadow mask opening. If this scattered light is subsequently absorbed by the perovskite in those regions, it could lead to an overestimation of the J_{SC}. Indeed, the IPCE was observed to be slightly higher—particularly in the longer wavelength region,

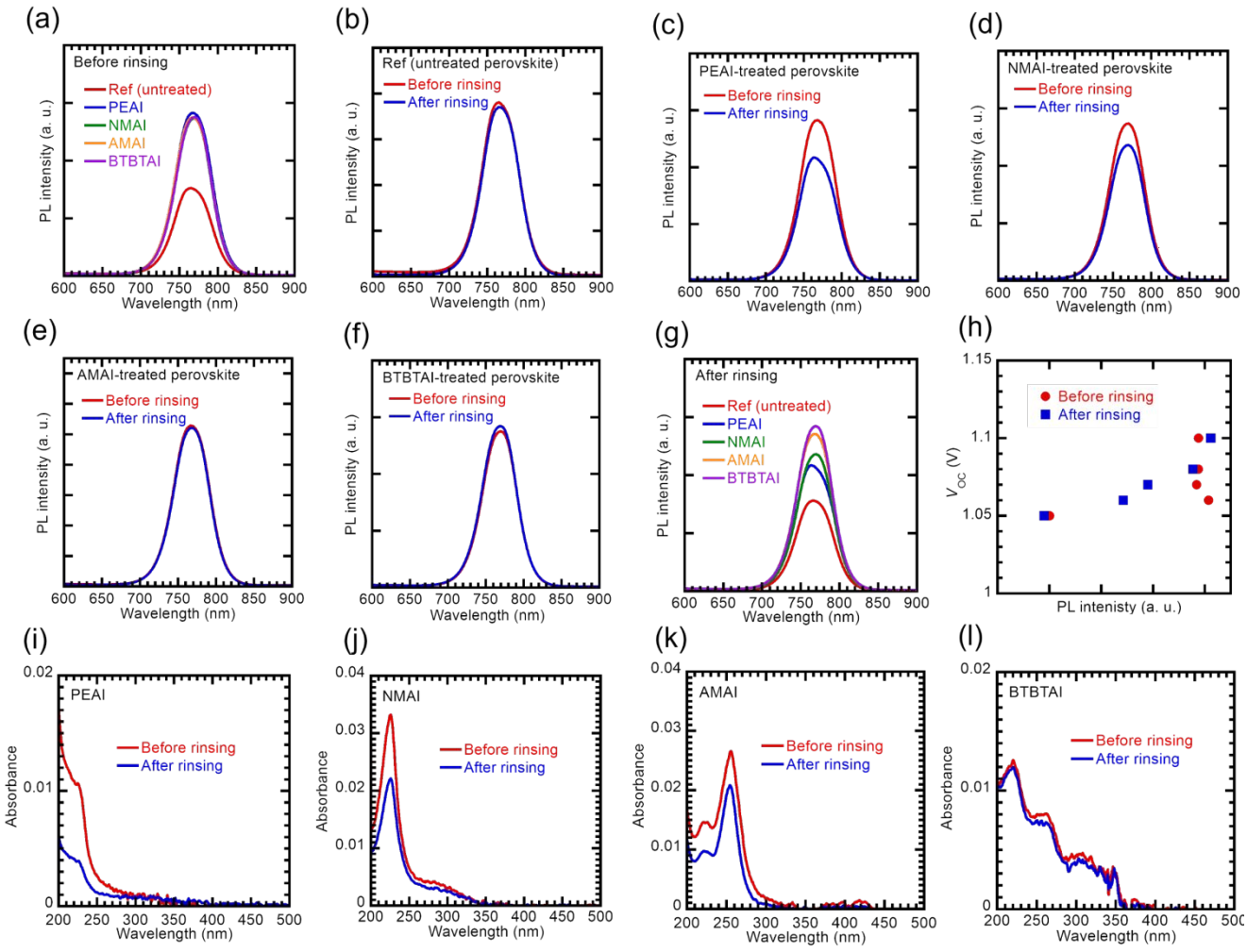

Fig. 3 (a) Steady-state PL spectra of untreated and surface-treated mixed cation-based perovskite films before CB rinsing. Steady-state PL spectra of (b) untreated, (c) PEAI-treated, (d) NMAI-treated, (e) AMAI-treated, and (f) BTBTAI-treated mixed cation-based perovskite films before and after CB rinsing. (g) PL spectra of untreated and surface-treated mixed cation-based perovskite films after CB rinsing. (h) Plots of V_{OC} as a function of PL intensity for untreated and surface-treated mixed cation-based perovskite films before and after CB rinsing. Absorption spectra of (i) PEAI, (j) NMAI, (k) AMAI, and (l) BTBTAI films before and after CB rinsing.

where light absorption by the perovskite weakens due to decreased absorbance—when a 2 mM BTBTAI solution was used, compared to the case with 1 mM (Fig. S16a†). This higher J_{SC} is likely attributable to the scattering effect. Furthermore, the thick BTBTAI structure may hinder hole extraction, resulting in the reduced FF. Based on these, the optimal BTBTAI solution concentration is believed to be 1 mM, providing a high PCE without significant J_{SC} overestimation or FF reduction.

Fig. S17 † shows the *J*–*V* curves of mixed cation-based PSCs treated with the 1 mM BTBTAI solution, measured in consecutive forward and reverse scans under the simulated one-sun illumination. The PCEs were slightly higher in the reverse scan (from 1.2 V to 0 V) at 19.9% compared to the forward scan (from 0 V to 1.2 V) at 19.3%. Therefore, the reverse scan was used for evaluating all the PSCs discussed throughout this work. MPPT was performed on mixed cation-based PSCs treated with the 1 mM BTBTAI solution to assess PCE stabilization (Fig. S18 †). The PCE stabilized within a few seconds after the simulated one-sun illumination commenced, reaching a value of 20.0%, which aligns well with the PCE from the *J*–*V* measurements. The J_{SC} value calculated from the IPCE curve for mixed cation-based PSCs treated with the 1 mM BTBTAI solution (Fig. S16b †) was 23.2 mA cm^{-2}, nearly matching the value estimated from the *J*–*V* curves (24.7 mA cm^{-2}). The bandgap calculated from the IPCE onset (Fig. S16c †) was approximately 1.58 eV, consistent with the reported bandgap for perovskites of similar composition[60,61] as well as the optical bandgap of 1.62 eV (Fig. S19 †).

3.2 Comparison of surface treatment materials

Based on the previous considerations, the concentration of 1 mM was determined to be optimal for BTBTAI-treated PSCs. Using this concentration, mixed cation-based PSCs treated with PEAI, NMAI, and AMAI were fabricated, and their photovoltaic

characteristics were compared with BTBTAI-treated devices. The reference devices refer to PSCs without any treatment. As shown in Fig. 2a–e and Table S2 † , all device parameters improved with treatment in the following order: reference devices < PEAI-treated devices < NMAI-treated devices < AMAI-treated devices < BTBTAI-treated devices, with the reasons for these improvements to be discussed later. Specifically, the PCE was 17.6% for reference devices, 18.2% for PEAI-treated devices, 19.2% for NMAI-treated devices, 19.9% for AMAI-treated devices, and 20.2% for BTBTAI-treated devices. For PEAI, widely used for defect passivation in PSCs, the reported solution concentrations range from 2 to 20 mM.[7,11,25,26,48] which are higher than the concentration used in this study (1 mM). In our case, the highest PCE was obtained at PEAI concentrations of 2 and 3 mM (18.4%) and was not significantly different from that of PSCs treated with the 1 mM PEAI concentration (18.2%) (Table S3 †).

To gain further insight into the improved performance, TPV decays of the mixed cation-based PSCs were measured. This was done using square-shaped photoexcitation from a white LED, with an oscilloscope measuring the voltage across a 100 kΩ resistor. The intensity and duration of the photoexcitation were 100 mW cm^{-2} and 50 ms, respectively. With the high resistance (100 kΩ), the PSCs operate near open-circuit conditions (no current flow), so the TPV signals contain information about electron and hole recombination in the PSCs. Longer TPV lifetimes indicate reduced charge-carrier recombination in the PSCs. As shown in Fig. 2f, the TPV decays were slower for higher-performance devices, suggesting that defect passivation is a likely cause of the improved performance due to the suppression of charge recombination. In general, reducing charge recombination through defect passivation can increase the quasi-Fermi level splitting, leading to a higher V_{OC}.[15,16] Indeed, the V_{OC} increased with the perovskite surface treatment as shown in Fig. 2c.

To explore another mechanism of the improved PSC performance, TPC measurements were performed on the same PSCs, using the same setup but with a lower resistance of 50 Ω. With this low resistance, the PSCs operate close to short-circuit conditions. Shorter TPC decays are preferable for solar cell operation, as they indicate more efficient charge-carrier extraction. PSCs with higher performance exhibited faster TPC decays (Fig. 2g), which points to improved hole extraction at the perovskite/spiro-OMeTAD interface. In our PSCs, the increases in J_{SC} and FF were observed (Fig. 2b and 2d), likely resulting from this improved hole extraction.

To clarify how different surface treatment materials affect PSC degradation, the operational durability of the mixed cation-based PSCs was evaluated at 25°C under continuous illumination from a 3,000 K white LED with an intensity of 100 mW cm^{-2}. The operation condition was MPPT. As shown in Fig. 2h, the untreated reference devices exhibited the poorest durability, while those with surface treatments, which provided higher PCE, led to significantly improved durability. The best durability was achieved in the BTBTAI-treated PSCs. The efficiency retention percentages after 1,000 hours of the continuous illumination were 49% for untreated devices, 59% for PEAI-treated devices, 67% for NMAI-treated devices, 74% for AMAI-treated devices, and 80% for BTBTAI-treated devices.

The operational durability of PSCs remains a challenging issue for the commercialization of this photovoltaic technology. PSC degradation is partly caused by external environmental factors, such as oxygen and moisture in the air.[62–67] However, the oxygen- and water-induced degradation is unlikely, as our devices are encapsulated. Our encapsulation, which uses a glass lid, UV-curing sealant, and a desiccant sheet, is highly reliable and can protect devices from oxygen and moisture in the air for at least 3,000 hours at 85% relative humidity and a temperature of 85°C.[68]

PSC degradation can occur even in the absence of water and oxygen. Due to the soft ionic nature of perovskite materials, positively or negatively charged defects, such as vacancies and interstitials, are mobile within PSCs under internal and external electric fields.[69,70] As a result, ion migration easily proceeds in the form of mobile charged defects. The movement of these defects is strongly accelerated by light illumination and elevated temperatures.[71,72] For example, corrosion of the perovskite layer, organic HTL, and Ag electrode by migrated reactive species, such as iodine, occurs in PSCs during operation[71,73]. Additionally, perovskite degradation is especially severe at high temperatures due to volatilization and loss of various organic and iodine species.[74,75] Migration and penetration of Au into the perovskite layer from the electrode also induces PSC performance degradation.[68,76] Although some of these reported degradation pathways may exist in our PSCs, they cannot explain the durability differences shown in Fig. 2h because the only variation in device architecture is the choice of surface treatment material. Numerous studies have shown that passivating perovskite defects enhances both efficiency and durability.[4,12,17,18] Therefore, as demonstrated in this study, using surface treatment materials with extended π-conjugation provides more effective defect passivation and enhanced durability.

3.3 Defect passivation

To further investigate the defect passivation behavior in more detail, steady-state PL measurements were employed. PL measurements on mixed cation-based perovskite films fabricated on fused silica substrates revealed that PL intensities increased after surface treatment with PEAI, NMAI, AMAI, and BTBTAI (Fig. 3a). However, the PL intensities of the treated samples were very similar to one another, despite being higher than those of the untreated films. This observation seems contrary to the fact that the V_{OC} and TPV decays systematically varied depending on the surface treatment materials. We hypothesize that this occurs because part of the treatment molecules desorbs from the perovskite surface during the spin-coating of the spiro-OMeTAD HTL.

To test this hypothesis, PL spectra of mixed cation-based perovskite films were measured both before and after being

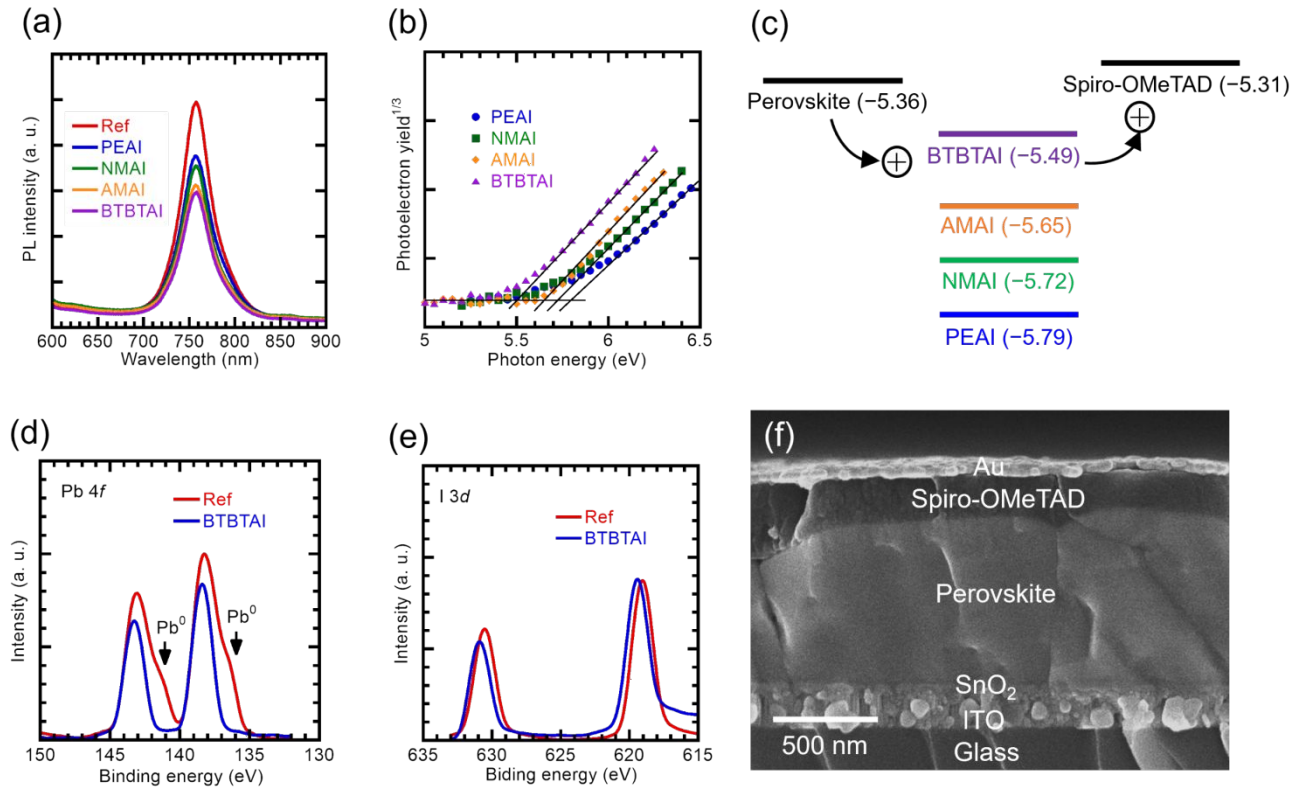

Fig. 4 (a) Steady-state PL spectra of untreated and surface-treated mixed cation-based perovskite films with chemically doped spiro-OMeTAD. (b) PYS plots for PEAI, NMAI, AMAI, and BTBTAI films. (c) Energy-level diagram illustrating hole extraction. XPS profiles of (d) Pb 4*f* and (e) I 3*d* for untreated and BTBTAI-treated mixed cation-based perovskite films. (f) Cross-sectional SEM image of mixed cation-based PSCs.

rinsed by spin-coating with pure CB, the solvent used for spiro-OMeTAD HTL fabrication. While untreated perovskite films showed no changes in their PL spectra before and after CB rinsing (Fig. 3b), the PL intensities of PEAI-treated films decreased after CB rinsing (Fig. 3c), likely due to the partial desorption of PEAI from the perovskite surface. In contrast, the reduction in PL intensity following CB rinsing was less pronounced for the other treated perovskite films (Fig. 3d–f). Notably, the BTBTAI-treated films exhibited almost no decrease in PL intensity even after CB rinsing (Fig. 3f), suggesting that BTBTAI's defect passivation effect remains intact even after rinsing. These results highlight that the desorption of surface treatment materials from perovskite layers poses a significant challenge to PSC performance, yet it has been a rarely explored area of research.[35–37]

The surface treatment molecules can interact with and anchor to the perovskite surfaces through the amino group to passivate defects. Since all the surface treatment materials investigated in this study have the same amino group, the anchoring strength shows little variation across all the materials as discussed later. In this context, the solubility of the surface treatment materials in organic solvents plays an additional role in their desorption behavior. We were unable to measure the solubility of the surface treatment materials in CB using the method of Fig. S15 † due to their extremely low solubility in CB. However, the solubility in CB is expected to decrease as the π-conjugation length increases, making them more resistant to desorption during the spin-coating of the spiro-OMeTAD HTL. Therefore, the PL data from the CB-rinsed perovskite films would reflect the more actual conditions in the PSCs. Indeed, the PL intensities of the CB-rinsed films exhibited a trend consistent with the PSC performance (Fig. 3g). Additionally, time-resolved transient PL decays were slower for the rinsed samples with higher steady-state PL intensities (Fig. S20 †). The V_{OC} values of the PSCs correlated well with the PL intensities of the rinsed samples, whereas no such correlation was observed before rinsing (Fig. 3h).

Experimentally observing surface treatment molecules anchored on the perovskite surface and their desorption behavior during CB rinsing is extremely challenging. Instead, thin films of PEAI, NMAI, AMAI, and BTBTAI were spin-coated from 1 mM solutions onto fused silica substrates, and their absorption spectra were measured before and after rinsing with CB. Although these molecules are not anchored to the fused silica substrate surfaces, making this system different from actual devices, we tentatively used this method to investigate molecular desorption behavior. Materials with shorter π-conjugation showed a greater reduction in absorbance after CB rinsing (Fig. 3i–k), while almost no reduction was observed for BTBTAI (Fig. 3l). This indirectly indicates that the surface

treatment molecules with more extended π-conjugation are less prone to desorption during the spin-coating of the HTL. Since the CB used in HTL spin-coating actually contains spiro-OMeTAD and dopants, it is important to note that the desorption behavior of surface treatment molecules is likely to differ from that observed with pure CB. These findings highlight the importance of selecting surface treatment materials with lower solubility in CB to maintain the original defect passivation effect, despite the challenges that lower solubility may pose when preparing high-concentration solutions for defect passivation.

It is possible that the lone pair of the sulfur atom in the BTBTAI molecule contributes to defect passivation by interacting with positively charged defects. However, when using BTBTAI, it is difficult to distinguish whether the observed defect passivation originates from the ammonium iodide group or from the sulfur atom's lone pair. To investigate this, a 0.5 nm-thick layer of C8-BTBT—sharing the same BTBT backbone as BTBTAI but lacking the ammonium iodide group—was vacuum-deposited onto the surface of a perovskite layer, and steady-state PL spectra were measured. An increase in PL intensity was observed after C8-BTBT deposition (Figure S21†), indicating that defect passivation by the sulfur atom's lone pair also occurs in the case of BTBTAI, thereby contributing to the improved PSC performance.

3.4 Perovskite film quality

To assess whether the surface treatment affects mixed cation-based perovskite film quality, their SEM images were taken. Tightly packed perovskite grains with diameters of hundreds of nanometers were observed, and the surface morphologies remained unchanged for all samples (Fig. S22 †). XRD patterns of untreated and treated perovskite films were also measured, showing almost no differences between samples (Figure S23 †). The peaks in the XRD patterns correspond to the three-dimensional perovskite structure and are consistent with previously reported data.[2,77,78] Additionally, the UV-VIS absorption spectra showed no dependence on surface treatments (Figure S24 †). Overall, the surface treatments did not have a detectable impact on perovskite film quality, serving primarily to passivate defects and enhance hole extraction.

3.5 Hole extraction behavior

The PL measurements also provide important insights into the hole extraction behavior at the perovskite/spiro-OMeTAD interface. After a mixed cation-based perovskite film was fabricated on a fused silica substrate and then surface-treated with PEAI, NMAI, AMAI, or BTBTAI, a chemically doped spiro-OMeTAD film was spin-coated on top of the perovskite film. PL spectra of the perovskite films covered with spiro-OMeTAD were then measured. In contrast to perovskite films without spiro-OMeTAD, lower PL intensities in the perovskite/spiro-OMeTAD stack samples indicate hole extraction from the perovskite film to the spiro-OMeTAD film. As shown in Fig. 4a, the surface treatments that led to higher PSC performance reduced PL intensities, indicating improved hole extraction. In these samples, the enhanced hole extraction, which reduces PL intensity, is believed to outweigh the effect of defect passivation, which would increase PL intensity. BTBTAI was found to be the most effective in improving hole extraction.

Perovskites' defects act as charge carrier recombination and trap centers, making it difficult for holes generated in the perovskite layer to cross the defective perovskite/spiro-OMeTAD interface due to hole trapping by the defects.[13,14] Surface treatments with PEAI, NMAI, AMAI, and BTBTAI can passivate these defects, thereby enhancing hole extraction. Another possible explanation for the improved hole extraction is the relative positions of energy levels in each surface treatment layer of the PSCs.

To evaluate the energy levels, PYS was performed on drop-cast films of PEAI, NMAI, AMAI, and BTBTAI. The hole transport energy levels measured using PYS were −5.79 eV for PEAI, −5.72 eV for NMAI, −5.65 eV for AMAI, and −5.49 eV for BTBTAI (Fig. 4b). The valence band edge energy level of the perovskite film and the hole transport energy level of the chemically doped spiro-OMeTAD film were also measured using PYS, yielding values of −5.36 eV and −5.31 eV, respectively (Figure S25a,b †).

An energy level diagram based on these values, measured using PYS, is shown in Fig. 4c. This diagram represents the case where each layer is not in contact; however, in reality, energy levels may shift due to interactions between the layers.[79–81] Although this concern exists, the diagram suggests that surface treatment materials with extended π-conjugation tend to exhibit shallower hole transport energy levels. PEAI, with its deepest energy level, hinders hole extraction from the perovskite layer to the spiro-OMeTAD layer, acting as an insulator for hole extraction in PSCs due to energy-level mismatching with the adjacent perovskite and spiro-OMeTAD layers. As surface treatment materials with shallower hole transport energy levels are used, energy-level mismatching is reduced, improving hole extraction through the treatment molecules and enhancing PSC performance. As discussed earlier, some surface treatment materials, such as PEAI and NMAI, desorb during the spin-coating of the spiro-OMeTAD HTL. This may result in direct hole extraction from the spiro-OMeTAD layer to the perovskite layer in areas where PEAI or NMAI, with deeper energy levels, desorbs. BTBTAI having the shallowest hole transport energy level and the lowest solubility delivers the best PSC performance by improving hole extraction and minimizing molecular desorption from the perovskite surface. However, the energy level of BTBTAI is deeper than those of perovskite and spiro-OMeTAD, meaning that the energy-level mismatch is not entirely eliminated. Using a surface treatment molecule with an even deeper energy level could potentially improve hole extraction further.

3.6 Interaction between BTBTAI molecules and the perovskite surface

The surface treatment materials investigated in this study can passivate defects by interacting to the perovskite surface through amino groups. To prove this, XPS analysis was performed, revealing that the Pb 4*f* and I 3*d* peaks shifted to

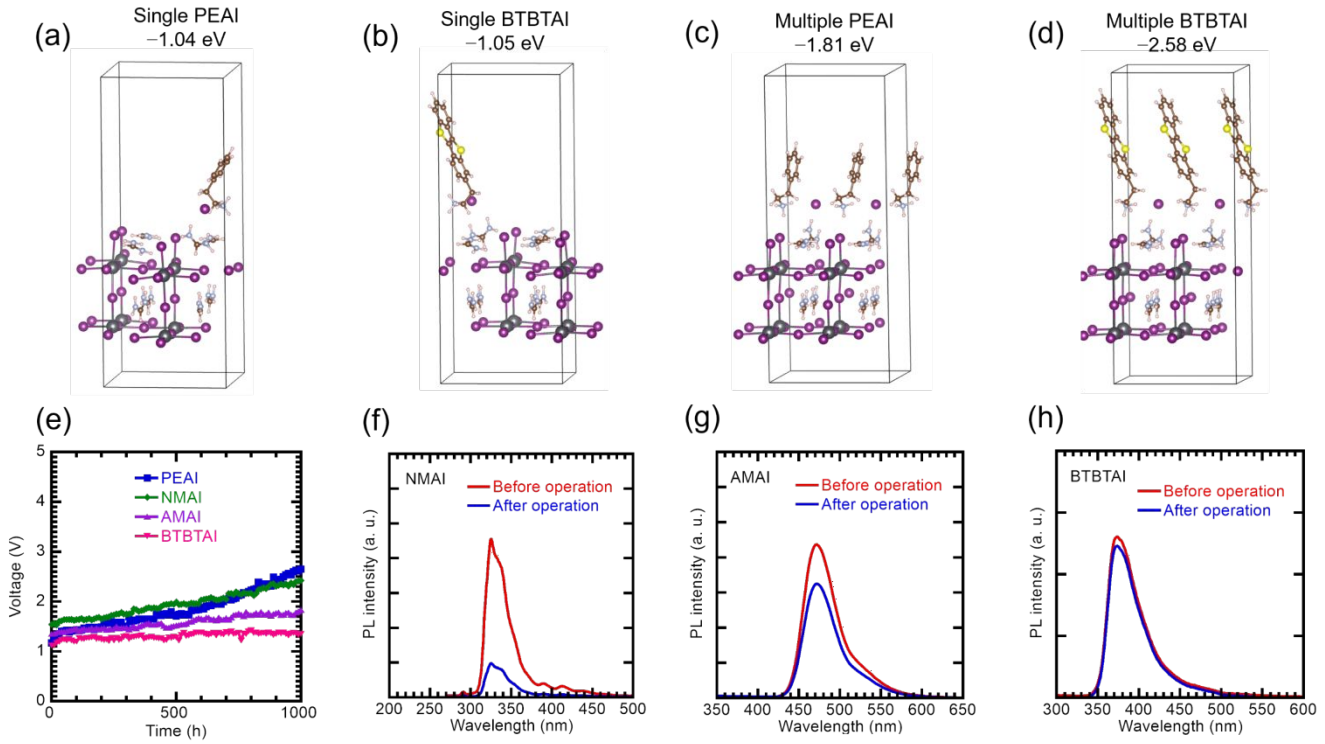

Fig. 5. Simulated molecular binding configurations and energies for (a) a single PEAI molecule, (b) a single BTBTAI molecule, (c) multiple PEAI molecules, and (d) multiple BTBTAI molecules on the $FAPbI_3$ perovskite surface. The binding energy values in (a–d) are given per molecule of PEAI and BTBTAI. (e) Voltage evolution of PEAI, NMAI, AMAI, and BTBTAI-based HODs under continuous operation at 25 mA cm^{-2}. Steady-state PL spectra of (f) NMAI, (g) AMAI, and (h) BTBTAI films before and after 1,000 hours of the HOD operation at 25

higher binding energies in BTBTAI-treated perovskite films compared with untreated films (Fig. 4d,e), indicating a change in the chemical environment of Pb^{2+} cations and I^- anions within the perovskite octahedral framework due to BTBTAI anchoring, consistent with literature reports.[82,83] Additionally, XPS peaks associated with metallic lead (possibly formed from Pb^{2+} cations) were observed in untreated perovskite samples. While the formation of Pb^0 due to X-ray photolysis is possible,[84] no metallic lead was detected in BTBTAI-treated films. There is a similar report of the Pb^0 peak disappearing due to defect passivation.[80,85] This suggests that BTBTAI molecules not only passivate perovskite defects but also suppress the formation of Pb^0, which is known to act as carrier recombination centers in PSCs.[86,87] Cross-sectional SEM analysis confirmed that the PSCs exhibited a well-structured multilayer architecture, with BTBTAI not clearly visible due to its very thin layer (Fig. 4f).

To investigate the binding interaction between the surface treatment molecules and the perovskite surface, density functional theory calculations were performed using the Vienna Ab initio Simulation Package. The Perdew–Burke–Ernzerhof exchange–correlation functional within the generalized gradient approximation was used, along with a 3×3×1 k-point mesh and a plane-wave energy cutoff of 520 eV for the models shown in Figure 5a–d. All atomic positions were fully relaxed. The supercell was constructed using a 2×2×2 array of primitive $FAPbI_3$ perovskite unit cells, with a 1.5 nm vacuum layer to prevent spurious interactions due to periodic boundary conditions. To preserve charge neutrality, the molecules were adsorbed on surfaces terminated with iodide anions. The cutoff energy and k-point sampling were confirmed to converge within an energy tolerance of 0.001 eV.

When a single PEAI or BTBTAI molecule was placed on the $FAPbI_3$ perovskite surface (Figure 5a and 5b), the calculated binding energies were –1.04 eV and –1.05 eV, respectively, indicating no significant difference. This similarity is attributed to the fact that both molecules share the same ammonium iodide anchoring group. However, when multiple molecules were placed on the perovskite surface and one of them was removed (Figure 5c and 5d), the calculated binding energies were –1.81 eV for PEAI and –2.58 eV for BTBTAI. These more negative values suggest stronger overall binding, likely due to additional stabilization from π–π interactions between adjacent molecules. The significantly stronger binding observed for BTBTAI is attributed to its enhanced π–π stacking capability resulting from its larger π-conjugated core. In combination with its lower solubility, these strong intermolecular interactions likely contribute to the reduced desorption of BTBTAI molecules during the subsequent HTL spin-coating.

Recently, 2D perovskite layers have been applied to the surfaces of 3D perovskite light-absorbing layers to achieve defect passivation and better energy level alignment, resulting in improved PSC performance.[28–30,88,89] However, it has also been reported that PSC performance decreases when a thick layer of 2D perovskite, with low bulk hole transport capability, is formed.[87,89] Thus, the formation of 2D perovskite layers on 3D

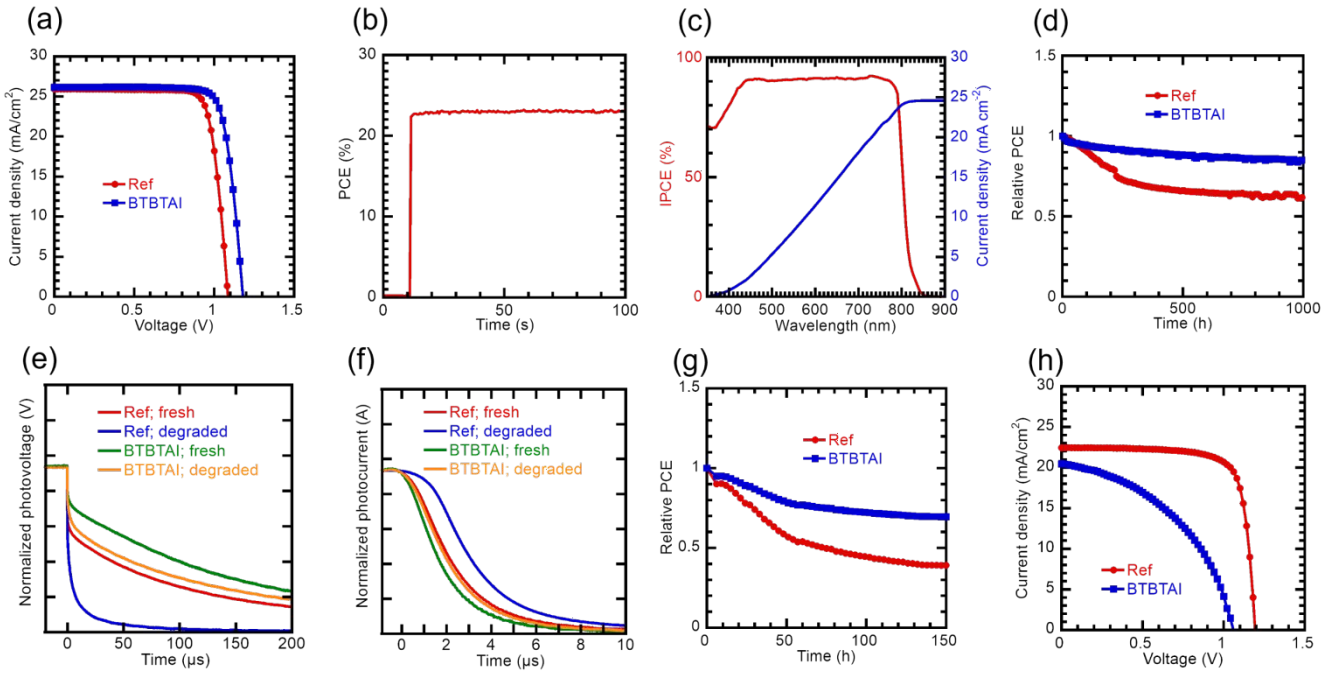

Fig. 6 (a) Representative illuminated *J*–*V* curves, (b) PCE stabilization behavior, (c) IPCE curve, and (d) PCE evolution under the continuous illumination with MPPT at 25 °C, (e) TPV and (f) TPC decays (measured before and after the operational durability test), and (g) PCE evolution under the continuous illumination with MPPT at 85 °C for $FAPbI_3$-based PSCs with and without BTBTAI treatment. (h) Representative illuminated *J*–*V* curves of $Cs_{0.05}FA_{0.8}MA_{0.15}PbI_{2.25}Br_{0.75}$-based inverted PSCs with and without BTBTAI treatment.

perovskite layers can have both positive and negative impacts on PSC performance. In the standard XRD measurement results shown in Fig. S23 †, no peaks associated with the BTBTAI-based lower-dimensional perovskite phase were observed. GIXRD, which is used to determine the crystalline structures of surfaces or thin films, also did not detect the lower-dimensional perovskite phase in BTBTAI-treated 3D perovskite films (Fig. S26 †). Based on time-of-flight secondary ion mass spectrometry and XPS measurements, the presence of BTBTAI in the PSC could not be confirmed, likely due to its extremely low concentration and the overlap of its constituent elements with those in other layers. However, considering the aforementioned XRD results showing no formation of 2D perovskite phases, it is inferred that BTBTAI does not penetrate into the perovskite bulk but instead remains on the perovskite surface.

3.7 Radical-cation stability

In the field of organic light-emitting diode research, many degradation pathways mediated by radical cations have been reported.[90–92] However, in PSCs, radical cation-mediated degradation has not been extensively discussed to date. Therefore, it is essential to investigate how radical-cation stability influences PSC performance. The HOMO states of the defect-passivation molecules were calculated using density functional theory. For computational simplicity, the molecules were modeled in their NH_3^+ state with the I^- counterion removed. The HOMO was found to be primarily localized not on the NH_3^+ group, but rather on the π-conjugated organic cores—such as benzene, anthracene, naphthalene, and BTBT (Fig. S27 †). This suggests that electron extraction and the formation of radical cations likely occur within these core regions.

To investigate the radical-cation stability, HODs with the architecture glass substrate/ITO (150 nm)/MoO_x (10 nm)/vacuum-deposited PEAI, NMAI, AMAI, or BTBTAI (200 nm)/MoO_x (10 nm)/Au (80 nm) were fabricated. The MoO_x layers, with their deep Fermi level of −5.94 eV (Fig. S25c †), enable efficient hole injection into PEAI, NMAI, AMAI, and BTBTAI. A constant current density of 25 mA cm^{-2}, which is close to the J_{SC} of the PSCs, was continuously applied to the HODs, and their voltages were monitored over time. The absolute voltage values at 0 hours varied between devices, likely due to differences in hole transport abilities of the bulk layers. However, in PSCs, the bulk transport plays a less significant role, as the PEAI, NMAI, AMAI, and BTBTAI molecules may form extremely thin layers—possibly monolayers—on the perovskite surfaces. As shown in Fig. 5e, the voltages at 25 mA cm^{-2} increased more slowly over time for HODs with more extended π-conjugation materials, with BTBTAI-based HODs showing the slowest voltage increase because of the high cation stability. The average voltage increase rates were 1.5 mV h^{-1} for PEAI-based HODs, 0.88 mV h^{-1} for NMAI-based HODs, 0.48 mV h^{-1} for AMAI-based HODs, and 0.23 mV h^{-1} for BTBTAI-based HODs. In all the HODs, no detectable crystallization was observed by visual inspection or optical microscopy after 1,000 hours of the operation.

After the operation, the encapsulation glass lid was removed from the HODs using a knife, and the upper Au electrode was

peeled off using Scotch tape. This de-encapsulation was necessary because glass and ITO do not transmit light at wavelengths below 300 nm, making it impossible to photoexcite PEAI, NMAI, and AMAI for PL measurements. PL spectra were then measured from the bare PEAI, NMAI, AMAI, and BTBTAI layers. For the PL measurements, excitation light was directed only onto the HOD driving area through a shadow mask with a circular aperture of 1 mm in diameter. Uncertainty remains regarding the possibility that part of the organic layer adhered to the peeled-off Au electrode, leading to variations in the organic layer's thickness and PL intensity. Based on our experience peeling away gold electrodes from PSCs using the same methods,[68,87] it is likely that delamination occurs between the poorly adhered gold electrode and the organic layer. Assuming that only the Au electrode was removed, leaving the organic layer intact on the substrate side, it was found that materials with longer π-conjugation lengths, except for PEAI, exhibited smaller reductions in PL intensity after 1,000 hours of the HOD operation (Fig. 5f–h). No PL was detected from the peeled gold electrode side, indirectly suggesting the absence of organic components on the electrode side, although it remains possible that any organic PL is quenched by the gold electrode. If exciton quenchers form during HOD degradation, even in small amounts, they could significantly reduce the PL intensity.[93,94] Additionally, such quenchers may act as hole trap sites, leading to the increase in the HOD's operating voltage. Across the wavelength range above 200 nm, PEAI showed no PL whatsoever, even in fresh, unoperated samples. However, the rapid HOD voltage increase shown in Fig. 5e suggests that PEAI, widely used for defect passivation in PSCs, is relatively unstable in its cationic state, limiting its effectiveness in improving PSC durability. The PL spectra of BTBTAI remained nearly unchanged before and after HOD operation (Fig. 5h), indicating that cation-induced degradation is unlikely for BTBTAI.

In general, cations are reactive,[38–44] so their interactions with other materials or electrodes may influence bulk hole transport or interfacial hole injection. However, radical cations become more stable with extended π-conjugation due to the delocalization of the radical cation across the molecule.[39,45–47] Therefore, employing molecules with extended π-conjugation can reduce reactivity and help suppress the increase in the HOD's voltage and the decrease in PL intensity, as shown in Fig. 5e–h. The stability of radical cations is also believed to influence the operational durability of PSCs. Given that PSCs contain highly reactive materials, such as halogens and chemical dopants, interactions between the cations and these reactive species likely occur. However, the specific radical cation-associated interactions that occur within PSCs during long-term operation remain unclear and require further investigation. Among the surface treatment molecules investigated, BTBTAI, with extended π-conjugation, forms stable radical cations, enhancing the durability of both HODs and PSCs.

3.8 BTBTAI treatment on $FAPbI_3$-based devices

To demonstrate the effectiveness of using BTBTAI treatment, PSCs with an alternative perovskite composition ($FAPbI_3$) were examined. As shown in Fig. 6a and Table S4 †, BTBTAI treatment on $FAPbI_3$-based devices increased the J_{SC} from 25.9 to 26.1 mA cm^{-2}, the V_{OC} from 1.09 to 1.14 V, the FF from 0.81 to 0.83, and the PCE from 22.7 to 24.6%. These improvements are attributed to enhanced defect passivation and hole extraction with BTBTAI as discussed earlier. In BTBTAI-treated PSCs, the PCE stabilized immediately after the simulated solar illumination began (Fig. 6b), and the J_{SC} derived from their IPCE curve (24.6 mA cm^{-2}) nearly aligned with that obtained from the *J*–*V* curves (Fig. 6c).

Additionally, the operational durability of $FAPbI_3$-based PSCs improved with BTBTAI treatment (Fig. 6d), increasing the PCE retention from 61% to 85% after 1,000 hours of the continuous white LED illumination under MPPT conditions at 25°C. The TPV and TPC measurements were conducted on $FAPbI_3$-based PSCs before and after the operational durability test. For the fresh samples, consistent with the previous discussion, BTBTAI treatment resulted in a slower TPV decay and a faster TPC decay (Fig. 6e and 6f). After the durability test, both untreated and BTBTAI-treated PSCs exhibited faster TPV decay and slower TPC decay, indicating enhanced carrier recombination and reduced hole extraction due to device degradation. However, in BTBTAI-treated PSCs, the decrease in TPV lifetime and the increase in TPC lifetime after degradation were both less pronounced, compared with the fresh PSCs (Table S5 and S6 †). These results further support that BTBTAI treatment suppresses degradation and improves device durability.

Furthermore, BTBTAI treatment was also found to enhance the durability of $FAPbI_3$-based PSCs under the light illumination at an elevated temperature of 85 °C (Fig. 6g). The PCE retention after 150 hours at 85 °C was 39% for the untreated PSCs and 70% for those treated with BTBTAI. These results clearly demonstrate that BTBTAI treatment is effective not only for the mixed cation-based perovskite but also for the $FAPbI_3$-based perovskite.

However, PSC performance decreased when BTBTAI treatment was applied to inverted PSCs with the architecture of glass substrate/ITO/NiO_x/Me-4PACz/$Cs_{0.05}FA_{0.8}MA_{0.15}PbI_{2.25}Br_{0.75}$ perovskite/C_{60}/BCP/Ag (Fig. 6h and Table S7 †). The electron transport energy level of BTBTAI is estimated at −2.09 eV by adding the absorption onset of 3.40 eV (Fig. 3l) to the hole transport energy level of −5.49 eV (Fig. 4c). This energy level significantly lies above those of the perovskite (−3.67 eV) and C_{60} (−4.35 eV),[58] indicating that electron extraction through BTBTAI is inefficient, resulting in the reduced PSC performance. This highlights the importance of appropriately selecting defect passivation molecules based on the specific device architecture.

Conclusions

This study investigates how solubility in organic solvents, hole transport energy levels, and the radical-cation stability of four surface treatment molecules with varying π-conjugation lengths (PEAI, NMAI, AMAI, and BTBTAI) influence defect passivation, hole extraction, and their combined effects on the PCE and

operational durability of PSCs. These molecules anchor to the perovskite surface through ammonium iodide groups, thus passivating defects. Our results show that increasing the π-conjugation length—from PEAI to NMAI, AMAI, and BTBTAI—enhances overall device performance. Surface treatment molecules with longer π-conjugation lengths exhibit lower solubility in organic solvents and enhanced intermolecular π–π stacking, limiting desorption from perovskite surfaces during spiro-OMeTAD HTL spin-coating and enabling more effective defect passivation. Additionally, surface treatment molecules with extended π-conjugation display shallower hole transport energy levels, reducing energy-level mismatches at interfaces and facilitating hole extraction, thereby boosting PCE. The radical-cation stability of surface treatment molecules is likely related to PSC operational durability, with longer π-conjugation molecules providing enhanced radical-cation stability and device durability. Among the materials tested, BTBTAI, with the most extended π-conjugation, demonstrates the best PSC performance by preventing molecular desorption, minimizing energy-level mismatches, and ensuring high radical-cation stability. Consequently, BTBTAI treatment raises the initial PCE from 22.7% to 24.6% and improves efficiency retention from 61% to 85% after 1,000 hours of continuous illumination at 25 °C in $FAPbI_3$-based PSCs. Although many studies report on defect passivation in PSCs, limited attention has been paid to solvent-induced desorption and radical-cation stability of surface treatment molecules. Thus, the findings of this study provide valuable insights into defect passivation and hole extraction, offering guidance for the design of future passivation molecules and PSC architectures. It is known that defect passivation ability varies with factors such as the introduction of functional substituents into the π-conjugated backbone, the position of the amino group, and the length of the carbon chain linking the amino group to the π-conjugated backbone.[26,48,95–97] These aspects have not yet been examined, and investigating them for BTBTAI, which performed best in this study, is part of our future plans.

Author contributions

D. K., C. A. M. S., D. S., Y. F., J. L., M. Z., Z. G. conducted sample fabrication, evaluation, and data analysis with the advice of S. I., H. S., and T. M., and T. B. R. and M. W. contributed the synthesis of the defect passivation materials. J. S. and A. S. performed calculations. D. K. and T. M. co-wrote the manuscript. All authors reviewed and approved the final manuscript.

Conflicts of interest

There are no conflicts to declare.

Data availability

The data that support the findings of this study are available from the corresponding author upon reasonable request.

Acknowledgements

This work was supported by Precursory Research for Embryonic Science and Technology (PRESTO), Japan Science and Technology Agency (JST) (grant number JPMJPR23H8); New Energy and Industrial Technology Development Organization (NEDO), the Green Innovation Fund Project (grant number 21578635); Science and Technology Research Partnership for Sustainable Development (SATREPS), JST (grant number JPMJSA2306); ASPIRE FOR RISING SCIENTISTS, Adopting Sustainable Partnerships for Innovative Research Ecosystem (ASPIRE) (grant number JPMJAP2332), JST; JSPS KAKENHI (grant numbers 20H02817 and 24H00486); the Murata Science Foundation; the Iwatani Naoji Foundation; the Asahi Glass Foundation; and Mitsui Chemicals, Inc.—Carbon Neutral Research Center (MCI-CNRC), International Institute for Carbon-Neutral Energy Research (WPI-I2CNER), Kyushu University.

References

1 National renewable energy laboratory. Best research-cell efficiency chart. https://www.nrel.gov/pv/cell-efficiency.html, *(Accessed: April 18, 2025)*.

2 J. Jeong, M. Kim, J. Seo, H. Lu, P. Ahlawat, A. Mishra, Y. Yang, M. A. Hope, F. T. Eickemeyer, M. Kim, Y. J. Yoon, I. W. Choi, B. P. Darwich, S. J. Choi, Y. Jo, J. H. Lee, B. Walker, S. M. Zakeeruddin, L. Emsley, U. Rothlisberger, A. Hagfeldt, D. S. Kim, M. Grätzel and J. Y. Kim, *Nature*, 2021, **592**, 381–385.

3 R. He, W. Wang, Z. Yi, F. Lang, C. Chen, J. Luo, J. Zhu, J. Thiesbrummel, S. Shah, K. Wei, Y. Luo, C. Wang, H. Lai, H. Huang, J. Zhou, B. Zou, X. Yin, S. Ren, X. Hao, L. Wu, J. Zhang, J. Zhang, M. Stolterfoht, F. Fu, W. Tang and D. Zhao, *Nature*, 2023, **618**, 80–86.

4 J. Suo, B. Yang, E. Mosconi, D. Bogachuk, T. A. S. Doherty, K. Frohna, D. J. Kubicki, F. Fu, Y. J. Kim, O. Er-Raji, T. Zhang, L. Baldinelli, L. Wagner, A. N. Tiwari, F. Gao, A. Hinsch, S. D. Stranks, F. De Angelis and A. Hagfeldt, *Nat. Energy*, 2024, **9**, 172–183.

5 H. Liu, J. Wang, Y. Qu, H. Zhou, Y. Xia, Y. Shi, R. Chen, T. Shi, S. De Wolf, W. Zhang and H.-L. Wang, *ACS Energy Lett.*, 2024, **9**, 2790–2799.

6 T. Ohsawa, N. Shibayama, N. Nakamura, S. Tamura, A. Hayakawa, Y. Murayama, K. Makisumi, M. Kitahara, M. Takayama, T. Matsui, A. Okuda, Y. Nakamura, M. Ikegami and T. Miyasaka, *J. Mater. Chem. A*, 2024, **12**, 22510–22515.

7 Q. Jiang, Y. Zhao, X. Zhang, X. Yang, Y. Chen, Z. Chu, Q. Ye, X. Li, Z. Yin and J. You, *Nat. Photon.*, 2019, **13**, 460–466.

8 C. Fei, A. Kuvayskaya, X. Shi, M. Wang, Z. Shi, H. Jiao, T. J. Silverman, M. Owen-Bellini, Y. Dong, Y. Xian, R. Scheidt, X. Wang, G. Yang, H. Gu, N. Li, C. J. Dolan, Z. J. D. Deng, D. N. Cakan, D. P. Fenning, Y. Yan, M. C. Beard, L. T. Schelhas, A. Sellinger and J. Huang, *Science*, 2024, **384**, 1126–1134.

9 Q. Jiang, R. Tirawat, R. A. Kerner, E. A. Gaulding, Y. Xian, X. Wang, J. M. Newkirk, Y. Yan, J. J. Berry and K. Zhu, *Nature*, 2023, **623**, 313–318.

10 S. Tan, C. Li, C. Peng, W. Yan, H. Bu, H. Jiang, F. Yue, L. Zhang, H. Gao and Z. Zhou, *Nat. Commun.*, 2024, **15**, 4136.

11 S. Xiong, F. Tian, F. Wang, A. Cao, Z. Chen, S. Jiang, D. Li, B. Xu, H. Wu, Y. Zhang, H. Qiao, Z. Ma, J. Tang, H. Zhu, Y. Yao, X. Liu, L. Zhang, Z. Sun, M. Fahlman, J. Chu, F. Gao and Q. Bao, *Nat. Commun.*, 2024, **15**, 5607.

12 C. Zhang, X. Shen, M. Chen, Y. Zhao, X. Lin, Z. Qin, Y. Wang and L. Han, *Adv. Energy Mater.*, 2023, **13**, 2203250.

13 S. Bera, A. Saha, S. Mondal, A. Biswas, S. Mallick, R. Chatterjee and S. Roy, *Mater. Adv.*, 2022, **3**, 5234–5247.

14 Z. Guo, M. Yuan, G. Chen, F. Liu, R. Lu and W. Yin, *Adv. Sci.*, 2024, **11**, 2305799.

15 P. Caprioglio, M. Stolterfoht, C. M. Wolff, T. Unold, B. Rech, S. Albrecht and D. Neher, *Adv. Energy Mater.*, 2019, **9**, 1901631.

16 K. Kearney, G. Seo, T. Matsushima, C. Adachi, E. Ertekin and A. Rockett, *J. Am. Chem. Soc.*, 2018, **140**, 15655–15660.

17 Z. Qu, Y. Zhao, F. Ma, L. Mei, X. K. Chen, H. Zhou, X. Chu, Y. Yang, Q. Jiang, X. Zhang and J. You, *Nat. Commun.*, 2024, **15**, 8620.

18 J. Xia, C. Liang, S. Mei, H. Gu, B. He, Z. Zhang, T. Liu, K. Wang, S. Wang, S. Chen, Y. Cai and G. Xing, *J. Mater. Chem. A*, 2021, **9**, 2919–2927.

19 Y. Li, X. Song, F. Deng, Y. Wang, Y. Yu, X. Han and X. Tao, *ACS Appl. Mater. Interfaces*, 2023, **15**, 48207–48215.

20 J. Fang, L. Wang, Z. Chen, S. Wang, L. Yuan, A. Saeed, I. Hussain, J. Zhao, R. Liu and Q. Miao, *ACS Appl. Mater. Interfaces*, 2024, **16**, 23443–23451.

21 L. Guan, N. Jiao and Y. Guo, *J. Phys. Chem. C*, 2019, **123**, 14223–14228.

22 J. K. Mishra, N. Yantara, A. Kanwat, T. Furuhashi, S. Ramesh, T. Salim, N. F. Jamaludin, B. Febriansyah, Z. E. Ooi, S. Mhaisalkar, T. C. Sum, K. Hippalgaonkar and N. Mathews, *ACS Appl. Mater. Interfaces*, 2022, **14**, 34238–34246.

23 Z.-E. Shi, J.-Y. Long, C.-W. Li, S.-Y. Hsieh, Y.-S. Hsiao, C.-P. Chen and Y.-H. Yu, *Sustain. Energy Fuels*, 2022, **6**, 1950–1958.

24 L. Fu, H. Li, L. Wang, R. Yin, B. Li and L. Yin, *Energy Environ. Sci.*, 2020, **13**, 4017–4056.

25 Y. S. Lee, J. Jae Do and J. W. Jung, *J. Alloys Compd.*, 2024, **988**, 174060.

26 H. Zhu, Y. Liu, F. T. Eickemeyer, L. Pan, D. Ren, M. A. Ruiz-Preciado, B. Carlsen, B. Yang, X. Dong, Z. Wang, H. Liu, S. Wang, S. M. Zakeeruddin, A. Hagfeldt, M. I. Dar, X. Li and M. Grätzel, *Adv. Mater.*, 2020, **32**, 1907757.

27 E. Choi, J. Lee, M. Anaya, A. Mirabelli, H. Shim, J. Strzalka, J. Lim, S. Yun, M. Dubajic, J. Lim, J. Seidel, R. E. Agbenyeke, C. G. Kim, N. J. Jeon, A. M. Soufiani, H. H. Park and J. S. Yun, *Adv. Energy Mater.*, 2023, **13**, 2301717.

28 E. Shi, B. Yuan, S. B. Shiring, Y. Gao, Akriti, Y. Guo, C. Su, M. Lai, P. Yang, J. Kong, B. M. Savoie, Y. Yu and L. Dou, *Nature*, 2020, **580**, 614–620.

29 E. Shirzadi, F. Ansari, H. Jinno, S. Tian, O. Ouellette, Felix. T. Eickemeyer, B. Carlsen, A. Van Muyden, H. Kanda, N. Shibayama, F. F. Tirani, M. Grätzel, A. Hagfeldt, M. K. Nazeeruddin and P. J. Dyson, *ACS Energy Lett*, 2023, **8**, 3955–3961.

30 F. Zhang, S. Y. Park, C. Yao, H. Lu, S. P. Dunfield, C. Xiao, S. Uličná, X. Zhao, L. Du Hill, X. Chen, X. Wang, L. E. Mundt, K. H. Stone, L. T. Schelhas, G. Teeter, S. Parkin, E. L. Ratcliff, Y.-L. Loo, J. J. Berry, M. C. Beard, Y. Yan, B. W. Larson and K. Zhu, *Science*, 2022, **375**, 71–76.

31 Y. Gao, E. Shi, S. Deng, S. B. Shiring, J. M. Snaider, C. Liang, B. Yuan, R. Song, S. M. Janke, A. Liebman-Peláez, P. Yoo, M. Zeller, B. W. Boudouris, P. Liao, C. Zhu, V. Blum, Y. Yu, B. M. Savoie, L. Huang and L. Dou, *Nat. Chem.*, 2019, **11**, 1151–1157.

32 S. You, F. T. Eickemeyer, J. Gao, J.-H. Yum, X. Zheng, D. Ren, M. Xia, R. Guo, Y. Rong, S. M. Zakeeruddin, K. Sivula, J. Tang, Z. Shen, X. Li and M. Grätzel, *Nat. Energy*, 2023, **8**, 515–525.

33 H. Chen, A. Maxwell, C. Li, S. Teale, B. Chen, T. Zhu, E. Ugur, G. Harrison, L. Grater, J. Wang, Z. Wang, L. Zeng, S. M. Park, L. Chen, P. Serles, R. A. Awni, B. Subedi, X. Zheng, C. Xiao, N. J. Podraza, T. Filleter, C. Liu, Y. Yang, J. M. Luther, S. De Wolf, M. G. Kanatzidis, Y. Yan and E. H. Sargent, *Nature*, 2023, **613**, 676–681.

34 G. M. Kim, H. Sato, Y. Ohkura, A. Ishii and T. Miyasaka, *Adv. Energy Mater.*, 2022, **12**, 2102856.

35 H. Zhang, Y. Wu, C. Shen, E. Li, C. Yan, W. Zhang, H. Tian, L. Han and W. Zhu, *Adv. Energy Mater.*, 2019, **9**, 1803573.

36 D. W. deQuilettes, S. Koch, S. Burke, R. K. Paranji, A. J. Shropshire, M. E. Ziffer and D. S. Ginger, *ACS Energy Lett.*, 2016, **1**, 438–444.

37 T. Wu, T. B. Raju, J. Shang, L. Wu, J. T. Song, C. A. M. Senevirathne, A. Staykov, S. Wang, S. Ida, N. Shibayama, T. Miyasaka, T. Matsushima and Z. Guo, *Adv. Mater.*, 2024, 2414576.

38 R. Mondal, C. Tönshoff, D. Khon, D. C. Neckers and H. F. Bettinger, *J. Am. Chem. Soc.*, 2009, **131**, 14281–14289.

39 B. Tang, J. Zhao, J.-F. Xu and X. Zhang, *Chem. Sci.*, 2020, **11**, 1192–1204.

40 Y. Kim, J. E. Byeon, G. Y. Jeong, S. S. Kim, H. Song and E. Lee, *J. Am. Chem. Soc.*, 2021, **143**, 8527–8532.

41 N. H. Attanayake, T. M. Suduwella, Y. Yan, A. P. Kaur, Z. Liang, M. S. Sanford and S. A. Odom, *J. Phys. Chem. C*, 2021, **125**, 14170–14179.

42 N. A. Romero and D. A. Nicewicz, *Chem. Rev.*, 2016, **116**, 10075–10166.

43 Q.-S. Gu, Z.-L. Li and X.-Y. Liu, *Acc. Chem. Res.*, 2020, **53**, 170–181.

44 K. Matyjaszewski and J. Xia, *Chem. Rev.*, 2001, **101**, 2921–2990.

45 A. Gobbi and G. Frenking, *J. Am. Chem. Soc.*, 1994, **116**, 9275–9286.

46 A. Shimizu, Y. Hirao, K. Matsumoto, H. Kurata, T. Kubo, M. Uruichi and K. Yakushi, *Chem. Commun.*, 2012, **48**, 5629.

47 A. Matsuura, T. Nishinaga and K. Komatsu, *J. Am. Chem. Soc.*, 2000, **122**, 10007–10016.

48 H.-S. Yoo and N.-G. Park, *Sol. Energy Mater. Sol. Cells*, 2018, **179**, 57–65.

49 Y. Wang, T. Zhang, M. Kan, Y. Li, T. Wang and Y. Zhao, *Joule*, 2018, **2**, 2065–2075.

50 K. Du, Q. Tu, X. Zhang, Q. Han, J. Liu, S. Zauscher and D. B. Mitzi, *Inorg. Chem.*, 2017, **56**, 9291–9302.

51 M. Hatamvand, S. Gholipour, M. Chen, Y. Zhou, T. Jiang, Z. Hu, Y. Chen and W. Huang, *Chem. Eng. J.*, 2023, **460**, 141788.

52 W. T. M. Van Gompel, R. Herckens, P.-H. Denis, M. Mertens, M. C. Gélvez-Rueda, K. Van Hecke, B. Ruttens, J. D'Haen, F. C. Grozema, L. Lutsen and D. Vanderzande, *J. Mater. Chem. C*, 2020, **8**, 7181–7188.

53 P. Denis, M. Mertens, W. T. M. Van Gompel, A. Maufort, S. Mertens, Z. Wei, M. Van Landeghem, S. Gielen, B. Ruttens, D. Deduytsche, C. Detarvernier, L. Lutsen, F. Grozema, K. Vandewal and D. Vanderzande, *Adv. Opt. Mater.*, 2022, **10**, 2200788.

54 S. Lammar, W. Van Gompel, S. Lenaers, M. Mertens, H.-G. Boyen, D. Desta, A. Hadipour, L. Lutsen, D. Vanderzande, A. Krishna, Y. Abdulraheem, T. Aernouts and J. Poortmans, *J. Mater. Chem. C*, 2023, **11**, 8146–8153.

55 H. Ebata, T. Izawa, E. Miyazaki, K. Takimiya, M. Ikeda, H. Kuwabara and T. Yui, *J. Am. Chem. Soc.*, 2007, **129**, 15732–15733.

56 H. Minemawari, T. Yamada, H. Matsui, J. Tsutsumi, S. Haas, R. Chiba, R. Kumai and T. Hasegawa, *Nature*, 2011, **475**, 364–367.

57 F. Deng, X. Li, X. Lv, J. Zhou, Y. Chen, X. Sun, Y.-Z. Zheng, X. Tao and J.-F. Chen, *ACS Appl. Energy Mater.*, 2020, **3**, 401–410.

58 L. Yang, Z. Fang, Y. Jin, H. Feng, B. Deng, L. Zheng, P. Xu, J. Chen, X. Chen, Y. Zhou, C. Shi, W. Gao, J. Yang, X. Xu, C. Tian, L. Xie and Z. Wei, *Adv. Mater.*, 2024, **36**, 2311923.

59 H. Kanno, N. C. Giebink, Y. Sun and S. R. Forrest, *App. Phys. Lett.*, 2006, **89**, 023503.

60 X. Dong, L. Chao, T. Niu, Y. Li, P. Guo, W. Hui, L. Song, Z. Wu and Y. Chen, *Solar RRL*, 2022, **6**, 2200060.

61 M. Wang, Y. Feng, Q. Dong, J. Bian, C. Wang, Y. Huang, C. Ma and Y. Shi, *Chem. Phys. Lett.*, 2019, **723**, 33–38.

62 B. Tan, S. R. Raga, A. S. R. Chesman, S. O. Fürer, F. Zheng, D. P. McMeekin, L. Jiang, W. Mao, X. Lin, X. Wen, J. Lu, Y. Cheng and U. Bach, *Adv. Energy Mater.*, 2019, **9**, 1901519.

63 G. Niu, W. Li, F. Meng, L. Wang, H. Dong and Y. Qiu, *J. Mater. Chem. A*, 2014, **2**, 705–710.

64 Y. Han, S. Meyer, Y. Dkhissi, K. Weber, J. M. Pringle, U. Bach, L. Spiccia and Y.-B. Cheng, *J. Mater. Chem. A*, 2015, **3**, 8139–8147.

65 N. Aristidou, C. Eames, I. Sanchez-Molina, X. Bu, J. Kosco, M. S. Islam and S. A. Haque, *Nat. Commun.*, 2017, **8**, 15218.

66 N. Aristidou, I. Sanchez-Molina, T. Chotchuangchutchaval, M. Brown, L. Martinez, T. Rath and S. A. Haque, *Angew. Chem.*, 2015, **127**, 8326–8330.

67 T. A. Berhe, W.-N. Su, C.-H. Chen, C.-J. Pan, J.-H. Cheng, H.-M. Chen, M.-C. Tsai, L.-Y. Chen, A. A. Dubale and B.-J. Hwang, *Energy Environ. Sci.*, 2016, **9**, 323–356.

68 B. Purev-Ochir, J. T. Song, P. Wang, M. Yahiro, S. Yamada, H. Nakanotani, T. Matsushima and C. Adachi, *Solar RRL*, 2024, **8**, 2400029.

69 O. Hentz, A. Singh, Z. Zhao and S. Gradečak, *Small Methods*, 2019, **3**, 1900110.

70 M. H. Futscher and C. Deibel, *ACS Energy Lett.*, 2022, **7**, 140–144.

71 J. M. Azpiroz, E. Mosconi, J. Bisquert and F. De Angelis, *Energy Environ. Sci.*, 2015, **8**, 2118–2127.

72 H. Baishya, R. Das Adhikari, M. J. Patel, D. Yadav, T. Sarmah, M. Alam, M. Kalita and P. K. Iyer, *J. Energy Chem.*, 2024, **94**, 217–253.

73 C. Eames, J. M. Frost, P. R. F. Barnes, B. C. O'Regan, A. Walsh and M. S. Islam, *Nat. Commun.*, 2015, **6**, 7497.

74 D. Wang, M. Wright, N. K. Elumalai and A. Uddin, *Sol. Energy Mater. Sol. Cells*, 2016, **147**, 255–275.

75 I. Deretzis, E. Smecca, G. Mannino, A. La Magna, T. Miyasaka and A. Alberti, *J. Phys. Chem. Lett.*, 2018, **9**, 3000–3007.

76 S. Guarnera, A. Abate, W. Zhang, J. M. Foster, G. Richardson, A. Petrozza and H. J. Snaith, *J. Phys. Chem. Lett.*, 2015, **6**, 432–437.

77 M. Saliba, T. Matsui, J.-Y. Seo, K. Domanski, J.-P. Correa-Baena, M. K. Nazeeruddin, S. M. Zakeeruddin, W. Tress, A. Abate, A. Hagfeldt and M. Grätzel, *Energy Environ. Sci.*, 2016, **9**, 1989–1997.

78 G. Tumen-Ulzii, M. Auffray, D. Klotz, G. F. Harrington, X.-K. Chen, U. Balijapalli, V. Vediyappan, N. Nakamura, Z. Feng, K. Takekuma, Y. Fujita, P. Wang, S. Yamada, K. Tamada, M. Batmunkh, Y. L. Zhong, F. Mathevet, H. Salway, M. Anaya, S. D. Stranks, T. Matsushima and C. Adachi, *ACS Appl. Energy Mater.*, 2022, **5**, 15819–15827.

79 W.-T. Wang, C.-H. Chiang, Q. Zhang, Y. Mu, C.-G. Wu and S.-P. Feng, *ACS Energy Lett.*, 2024, **9**, 2982–2989.

80 Q. He, A. Chen, T. Zhang, X. Chen, X. Bian, G. Xu, S. Pan, T. Chen, J. Yu, Z. Zhang, H. Zhu, G. Lu, O. M. Bakr and J. Pan, *Cell Rep. Phys. Sci.*, 2024, **5**, 102030.

81 B. Wang, H. Li, Q. Dai, M. Zhang, Z. Zou, J. Brédas and Z. Lin, *Angew. Chem. Int. Ed.*, 2021, **60**, 17664–17670.

82 Y. Guo, S. Apergi, N. Li, M. Chen, C. Yin, Z. Yuan, F. Gao, F. Xie, G. Brocks, S. Tao and N. Zhao, *Nat. Commun.*, 2021, **12**, 644.

83 C. Li, N. Zhang and P. Gao, *Mater. Chem. Front.*, 2023, **7**, 3797–3802.

84 J. D. McGettrick, K. Hooper, A. Pockett, J. Baker, J. Troughton, M. Carnie and T. Watson, *Mater Lett*, 2019, **251**, 98–101.

85 Z. Guo, S. Zhao, N. Shibayama, A. Kumar Jena, I. Takei and T. Miyasaka, *Adv. Funct. Mater.*, 2022, **32**, 2207554.

86 E. J. Juarez-Perez, L. K. Ono, M. Maeda, Y. Jiang, Z. Hawash and Y. Qi, *J. Mater. Chem. A*, 2018, **6**, 9604–9612.

87 G. Tumen-Ulzii, C. Qin, D. Klotz, M. R. Leyden, P. Wang, M. Auffray, T. Fujihara, T. Matsushima, J. Lee, S. Lee, Y. Yang and C. Adachi, *Adv. Mater.*, 2020, **32**, 1905035.

88 K. Mao, F. Cai, Z. Zhu, H. Meng, T. Li, S. Yuan, J. Zhang, W. Peng, J. Xu, X. Feng, Q. Chen and J. Xu, *Adv. Energy Mater.*, 2023, **13**, 2302132.

89 S. Sidhik, Y. Wang, M. De Siena, R. Asadpour, A. J. Torma, T. Terlier, K. Ho, W. Li, A. B. Puthirath, X. Shuai, A. Agrawal, B. Traore, M. Jones, R. Giridharagopal, P. M. Ajayan, J. Strzalka, D. S. Ginger, C. Katan, M. A. Alam, J. Even, M. G. Kanatzidis and A. D. Mohite, *Science*, 2022, **377**, 1425–1430.

90 D. Y. Kondakov, T. D. Pawlik, W. F. Nichols and W. C. Lenhart, *J. Soc. Inf. Disp.*, 2008, **16**, 37–46.

91 S. Kim, H. J. Bae, S. Park, W. Kim, J. Kim, J. S. Kim, Y. Jung, S. Sul, S.-G. Ihn, C. Noh, S. Kim and Y. You, *Nat. Commun.*, 2018, **9**, 1211.

92 G. Sato, D. Son, T. Ito, F. Osawa, Y. Cho and K. Marumoto, *Phys. Status Solidi A*, 2018, **215**, 1700731.

93 S. Scholz, D. Kondakov, B. Lüssem and K. Leo, *Chem. Rev.*, 2015, **115**, 8449–8503.

94 A. S. D. Sandanayaka, T. Matsushima and C. Adachi, *J. Phys. Chem. C*, 2015, **119**, 23845–23851.

95 Q. Cheng, H. Xia, X. Li, B. Wang, Y. Li, X. Zhang, H. Zhang, Y. Zhang and H. Zhou, *Solar RRL*, 2022, **6**, 2100805.

96 Z. Gozukara Karabag, A. Karabag, U. Gunes, X. Gao, O. A. Syzgantseva, M. A. Syzgantseva, F. Varlioglu Yaylali, N. Shibayama, H. Kanda, A. I. Rafieh, R. C. Turnell-Ritson, P. J.

Dyson, S. Yerci, M. K. Nazeeruddin and G. Gunbas, *Adv. Energy Mater.*, 2023, **13**, 2302038.

97 J. Xue, R. Wang, X. Chen, C. Yao, X. Jin, K.-L. Wang, W. Huang, T. Huang, Y. Zhao, Y. Zhai, D. Meng, S. Tan, R. Liu, Z.-K. Wang, C. Zhu, K. Zhu, M. C. Beard, Y. Yan and Y. Yang, *Science*, 2021, **371**, 636–640.

The data that support the findings of this study are available from the corresponding author upon reasonable request.